

Adsorption of Aromatic Hydrocarbons and Ozone at Environmental Aqueous Surfaces

Robert Vácha,[†] Lukasz Cwiklik,[†] Jan Řezáč,[†] Pavel Hobza,[†] Pavel Jungwirth,^{*,†}
Kalliat Valsaraj,[‡] Stephan Bahr,^{§,||} and Volker Kempter[§]

Institute of Organic Chemistry and Biochemistry, Academy of Sciences of the Czech Republic and Center for Biomolecules and Complex Molecular Systems, Flemingovo nám. 2, 16610 Prague 6, Czech Republic, Cain Department of Chemical Engineering, Louisiana State University, Baton Rouge, Louisiana 70803-7303, Institut für Physik and Physikalische Technologien, Technische Universität Clausthal, Leibnizstr. 4, D-38678 Clausthal-Zellerfeld, Germany, and Institut für Physik, Universität Osnabrück, Barbarastr. 7, D-49076 Osnabrück

Received: December 17, 2007; Revised Manuscript Received: March 17, 2008

Adsorption of environmentally important aromatic molecules on a water surface is studied by means of classical and ab initio molecular dynamics simulations and by reflection–absorption infrared spectroscopy. Both techniques show strong activity and orientational preference of these molecules at the surface. Benzene and naphthalene, which bind weakly to water surface with a significant contribution of dispersion interactions, prefer to lie flat on water but retain a large degree of orientational flexibility. Pyridine is more rigid at the surface. It is tilted with the nitrogen end having strong hydrogen bonding interactions with water molecules. The degree of adsorption and orientation of aromatic molecules on aqueous droplets has atmospheric implications for heterogeneous ozonolysis, for which the Langmuir–Hinshelwood kinetics mechanism is discussed. At higher coverages of aromatic molecules the incoming ozone almost does not come into contact with the underlying aqueous phase. This may rationalize the experimental insensitivity of the ozonolysis on the chemical nature of the substrate on which the aromatic molecules adsorb.

I. Introduction

Polycyclic aromatic hydrocarbons (PAHs) are ubiquitous in the natural environment. They arise mainly from incomplete combustion of fossil fuels, automobile emissions, oil cracking, and natural sources such as forest fires and volcanoes. PAHs are hydrocarbons that have two or more fused benzene rings in any possible configuration. Those, which are atmospherically significant range from the smallest two-ring compound (naphthalene) up to seven fused aromatic rings (coronene). As a matter of fact, the building unit of PAHs, i.e., benzene, is of similar atmospheric relevance as well. Polycyclic aromatic hydrocarbons are typically nonreactive under normal atmospheric conditions (but react in the presence of appreciable concentrations of polluting reactive gases such as OH radical or ozone^{1,2}) and have low vapor pressures and aqueous solubilities. Among the PAHs, naphthalene has the highest vapor pressure and is predominantly present in the gas-phase, whereas most of the higher molecular weight PAHs are associated with atmospheric aerosols.³ PAHs are highly hydrophobic and tend to concentrate in organic rich environments such as soils, sediment, plants, and other biota. Being hydrophobic they also bioconcentrate in the lipids of fish, birds, and humans. Several of the PAHs are known or suspected carcinogens and teratogens. For example, benzo[a]pyrene in ambient air was found to be a causative agent that produces cancer in experimental animals. Therefore, their

environmental fate and transport behavior have received significant attention in the past 50 years.³

There also exist atmospherically relevant aromatic compounds that have a N, O, or S atom inserted into the ring structure, pyridine being one of the atmospherically most relevant examples. These heterocyclic aromatic compounds (HAC) were found in the atmosphere, originating from industrial emissions (production of insecticides and herbicides) and coal combustion.^{4–8} In addition, the protonated ions of pyridine and its derivatives have been observed at significant levels in measurements of the background ion composition of the lower troposphere. Similarly to PAHs, HACs have a potential for atmospheric oxidation.⁹ For completeness, Table 1 summarizes atmospherically relevant physicochemical properties of pyridine, in comparison with benzene and naphthalene.

The behavior of PAHs at the air–water interface has been of considerable interest in recent years due to their potential for uptake and reaction on water droplets, thin water, and organic films on atmospheric aerosols, fog, and mist.^{10–15} Molecular dynamics simulations have shown that there is a deep free energy minimum at the air–water interface for PAHs, as well as for benzene, as the aromatic species migrates from the gas-phase into the aqueous phase.¹⁵ This free energy minimum was found to get deeper as the size of the PAH increased; in other words, the air–water interface partition constant increased. Experimentally, the trend was confirmed and there was good agreement between the predicted and observed values of the free energy of adsorption from the gas phase.¹⁵ The highly favorable nature of the air–water interface toward adsorption of high molecular weight PAH molecules from the gas phase also means that heterogeneous reactions at the interface are facilitated. In particular, this concerns oxidation of adsorbed PAH molecules by atmospheric oxidants such as ozone,

* To whom correspondence should be addressed. E-mail: pavel.jungwirth@uochb.cas.cz.

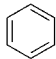
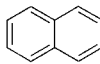
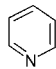
[†] Academy of Sciences of the Czech Republic and Center for Biomolecules and Complex Molecular Systems.

[‡] Louisiana State University.

[§] Technische Universität Clausthal.

^{||} Universität Osnabrück.

TABLE 1: Physicochemical Properties and Atmospheric Lifetimes for Compounds^a

Compound	Structure	Mol. Wt.	Aqueous Solubility/ mol.m ⁻³	Vapor pressure/ kPa	Atmospheric lifetime τ (d)
Benzene		78	23	0.12	4.8
Naphthalene		128	0.87	0.037	0.26
Pyridine		79		2.6	1.2

^aBased on average values of atmospheric concentrations and reported homogeneous gas-phase reaction rate constants of compounds with OH, O₃, and NO₃ species in the atmosphere: [OH] = 2 × 10⁶ molecules cm⁻³, [O₃] = 7 × 10¹¹ molecules cm⁻³, and [NO₃] = 5 × 10⁸ molecules cm⁻³. First order rate constants for compounds obtained from Ref. (Finlayson-Pitts and Pitts 2000). Atmospheric lifetime defined as 1/(Σ_ik_i[X_i]). Note that in the gas-phase the reaction is dominated by the OH radical.

hydroxyl radical, and nitrate radical to produce highly toxic oxy- and nitro-PAH compounds.^{1,2,16} These surface reactions have been directly observed and reported.^{11,14} Several recent studies have further shown that gas phase PAH molecules also adsorb to a variety of other surfaces (soot, organic films, inorganic silica, etc.).^{10,11,13}

The way of adsorption of these aromatic compounds on water including orientational effects can profoundly affect their reactivity (e.g., oxidation) on the surface. Whereas benzene and PAH compounds can have specific structural orientations on the aqueous surface due to interactions between water dangling hydrogens and aromatic rings, much less is known about the orientational effects of HACs (which contain polar C–N, C–O, or C–S bonds) at the air–water interface.

Here, we attempted to obtain further insight at the mechanism of adsorption of a typical PAH (naphthalene), benzene and pyridine at aqueous surfaces and at elucidating conditions for reaction of naphthalene with ozone combining computational and experimental approaches. We performed molecular dynamics (MD) simulations of coadsorption of naphthalene and ozone at an extended aqueous surface to address the following question: How do the reactants adsorb at the water surface and what is the probability of encounters between them? Based on the computational results, we rationalize experimental data concerning surface reactivity.

In addition we analyze by means of classical and ab initio MD simulations, as well as using vibrational spectroscopy for interaction of aromatic molecules with surfaces of amorphous solid water (ASW) the surface structure and orientation of benzene (as the building block of PAHs) and pyridine at varying surface concentrations. Nonvolatile ASW instead of volatile liquid water is employed since an ultrahigh vacuum chamber is used for combined photoelectron and vibrational spectroscopic investigation. The justification for comparing simulations of liquid water with experiments carried out on ASW is that the free energy profiles for the interaction of various organic molecules with liquid water and ASW are similar to each other as long as the adsorbate remains located above or at the surface.¹⁷ This indicates that the local disorder is the same on both substrates, and, indeed, results obtained for the interaction of aromatic molecules with liquid water surfaces can be semiquantitatively compared with experimental data obtained on water surfaces of much lower temperatures. The main

difference is that the adsorbed molecule is more mobile and flexible at elevated temperatures.

The rest of the paper is organized as follows. In section II we outline the possible surface reaction mechanisms. Sections III and IV provide computational and experimental details. Results and discussion are presented in section IV, whereas section V contains conclusions.

II. Surface Reaction Mechanisms

Reaction of adsorbed PAHs with ozone from the gas phase on different surfaces has been analyzed using a standard Langmuir–Hinshelwood mechanism.^{1,10,18} This assumes that the PAH and ozone adsorb independently at the air/water interface and reaction occurs between adsorbed molecules. This gives rise to a surface reaction rate of the form^{1,2}

$$-r_s = k_{II}^s \Gamma_{O_3} \Gamma_{PAH} \quad (1)$$

where r_s is given in molecule cm⁻² s⁻¹. k_{II}^s is the second order surface reaction rate constant (cm² molecule⁻¹ s⁻¹), Γ_{O_3} is the surface concentration of ozone (molecule cm⁻²), and Γ_{PAH} is the surface concentration of PAH (molecule cm⁻²). In most experiments, the conditions are such that the adsorption is linear in the PAH concentration and nonlinear in ozone concentration. In fact, the adsorption of ozone was assumed to be Langmuir-type in nature. Thus the overall reaction rate is given by¹⁶

$$-r_s = \frac{k_{II}^s \Gamma_{max} [O_3]}{C_{1/2} + [O_3]} \Gamma_{PAH} \quad (2)$$

with Γ_{max} and $C_{1/2}$ being the monolayer ozone adsorption capacity (molecule cm⁻²) and the gas-phase ozone concentration at half-saturation (molecule cm⁻³), respectively. $[O_3]$ is the gas-phase ozone concentration (molecule cm⁻³). The observed first order reaction rate constant (s⁻¹) is given by

$$k_{obs} = \frac{k_{II}^s \Gamma_{max} [O_3]}{C_{1/2} + [O_3]} \quad (3)$$

To obtain the surface reaction rate constant from the above equation, a fit of k_{obs} versus $[O_3]$ is made. The slope in the linear range is $k_{II}^s \Gamma_{max}$ which is used to obtain k_{II}^s (cm² molecule⁻¹ s⁻¹). This requires, however, a precise knowledge of Γ_{max} .

In cases when the monolayer adsorption capacity is either unknown or imprecisely known, a different approach is used. One defines an overall rate similar to that for gas-phase reactions¹⁹

$$-r_v = k_{II} [O_3] \Gamma_{PAH} \quad (4)$$

where, r_v is in molecule cm⁻³ s⁻¹. k_{II} is the second order reaction rate constant (molecule⁻¹ cm³s⁻¹), and $[O_3]$ is the gas-phase ozone concentration. The observed first-order reaction rate constant is given by

$$k_{obs}' = k_{II} [O_3] \quad (5)$$

Thus, we can define an ozone-normalized rate constant k_{II} . Note that this approach does not strictly employ any specific mechanism to arrive at the above equation and an Eley–Rideal mechanism can also give a similar rate expression.

Data on the rates of ozone reaction with a variety of PAHs on different surfaces (water, octanol, decanol, soot, long-chain fatty acids on water, glass, silica, and graphite) have been reported by various investigators.^{1,2,11,12,14,19,20} Table 2 lists the second order rate constant, k_{II}^s for a variety of PAHs, and Figure 1 displays the second order rate constant, k_{II} for different PAHs

TABLE 2: Second Order Surface Rate Constant, k_{II}^s ($\text{cm}^2 \text{ molecule}^{-1} \text{ s}^{-1}$) for Ozone Reaction with Various PAHs on Different Adsorbents

adsorbent	adsorbate	$k_{II}^s/\text{cm}^2 \text{ molecule}^{-1} \text{ s}^{-1}$	ref
spark discharge soot	benzo[a]pyrene	$(2.6 \pm 0.8) \times 10^{-17}$	39, 34
water (planar surface)	anthracene	2.55×10^{-17}	10
1-octanol on water	anthracene	2.59×10^{-17}	10
1-octanol	benzo[a]pyrene	$(5.5 \pm 0.2) \times 10^{-17}$	41
1-decanol	anthracene	$(2.5 \pm 0.1) \times 10^{-17}$	41
	naphthalene	$(0.9 \pm 0.1) \times 10^{-17}$	
	pyrene	$(0.7 \pm 0.1) \times 10^{-17}$	
	phenanthrene	$(0.5 \pm 0.3) \times 10^{-17}$	
water (droplet)	phenanthrene	2.5×10^{-16}	12
stearic acid on water	anthracene	$(2.26 \pm 0.20) \times 10^{-17}$	9
octanoic acid on water	anthracene	$(1.11 \pm 0.12) \times 10^{-17}$	
hexanoic acid on water	anthracene	$(0.48 \pm 0.07) \times 10^{-17}$	
glass	unsaturated alkene SAMs	$(2 \pm 1) \times 10^{-17}$	42

on silica and graphite. From Figure 1 and Table 2, it is interesting to note that the values of the rate constant show little variation for specific PAHs between different adsorbents. For example, the anthracene rate constants at different surfaces vary only from 0.48×10^{-17} to 2.5×10^{-17} even when the composition of the underlying surfaces varies drastically. Thus the nature of the surface seems to have only a minor role on the rate constant of the reaction. This raises the possibility of special orientational or electron transfer effects that lead to the above observation. Thus, there is a need to understand the simultaneous adsorption of PAHs and ozone on the aqueous surface. In order to do so, we performed a series of MD and ab initio simulations of PAH and ozone at aqueous surfaces. We address below the basic assumptions that are valid for representing the PAHs reaction rates on aqueous surfaces.

III. Computational Details

Classical molecular dynamics simulations were performed using the program package Gromacs.²¹ For simulating ozone and naphthalene at the air/water interface, the system consisted of 809 SPC/E water molecules placed in a prismatic cell with extended z -axis of dimensions $29 \times 29 \times 209 \text{ \AA}$. After application of 3D periodic boundary conditions (which allow to account efficiently for long-range electrostatic interactions via the standard particle-mesh Ewald procedure), this yielded infinite water slabs with two water/vapor interfaces in the xy -

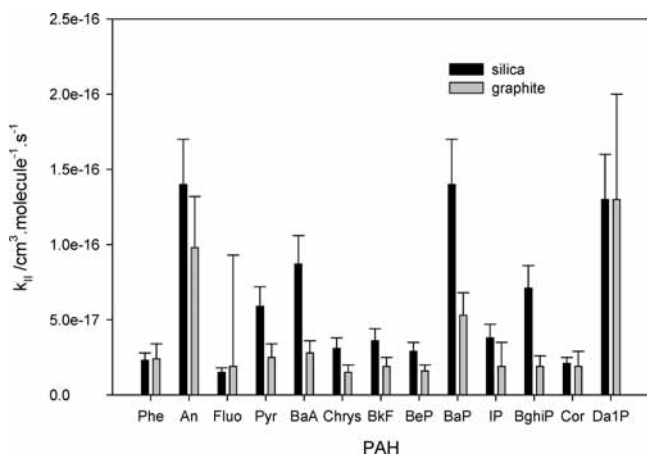


Figure 1. Ozone-normalized rate constant for reactions of particulate-adsorbed PAHs on different adsorbents.¹⁹ Phe, phenanthrene; An, anthracene; Fluo, fluoranthene; Pyr, pyrene; BaA, benz[a]anthracene; Chrs, chrysene; BkF, benzo[k]fluoranthene; BeP, benzo[e]pyrene; BaP, benzo[a]pyrene; IP, indeno[1,2,3-cd]pyrene; BghiP, benzo[g,h,i]pyrene; Cor, coronene; Da1P, dibenzo[a,1]pyrene.

plane. Further, we added to the simulation box varying amounts of ozone and naphthalene molecules with force-field parameters taken from refs 15 and 22. All these simulations were run in the NVT ensemble (i.e., with constant number of particles, volume, and temperature) at 300 K for 10 ns (with a time step of 1 fs) and configurations were saved every 2 ps.

In our analysis we assumed that the ozonolysis reaction rate is proportional to the number of contacts between reactants. A contact between ozone and naphthalene was defined as a configuration where two neighboring hydrogens of naphthalene were within 6.4 \AA from two side oxygens on ozone. This distance was determined from the corresponding radial distribution function as the position of first minimum after the first maximum (this minimum is, however, not well developed). Within reasonable margins the results do not strongly depend on this particular choice which we proved by performing the same analysis also using a 4 \AA distance criterion. Contacts between ozone and naphthalene were reexamined every two picoseconds and a lasting contact was then classified as a new one for the purpose of counting.

A similar slab system was employed to study the orientation of a single benzene or pyridine molecule on the water surface. For this we used 430 SPC/E water molecules²³ in the unit cell with dimensions $23 \times 23 \times 210 \text{ \AA}$. Potential parameters for benzene were taken from ref. 13, while for pyridine we initially adopted the OPLS-AA force-field.²⁴ However, the hydration free energy of pyridine (calculated using the potential of mean force method described in details in ref. 22) was only -3.8 kJ/mol , whereas the experimental values derived from Henry's law constant (taken from a compilation by Sander²⁵) were between -19.2 and -19.7 kJ/mol . Therefore, to obtain a pyridine model with proper hydration free energy we increased the charges on all atoms by 30%.

Results from classical MD of benzene and pyridine on a water slab were compared to those obtained from ab initio molecular dynamics simulations. The latter were performed with the CP2K/Quickstep program package which employs a density functional theory (DFT) approach with a mixed Gaussian and plane waves (GPW) approach.²⁶ The BLYP functional with the double- ζ valence polarized (DZVP) basis set was used. The energy cutoff for plane waves was set to 280 Ry and the Goedecker–Teter–Hutter pseudopotentials were applied.²⁷ In order to include dispersion interactions between an aromatic ring and water molecules (which are missing from common DFT functionals),^{28–30} we employed an empirical correction for density functional method (DFT+D).^{31–33}

The Quickstep source code was modified to include the dispersion correction calculation after electronic structure

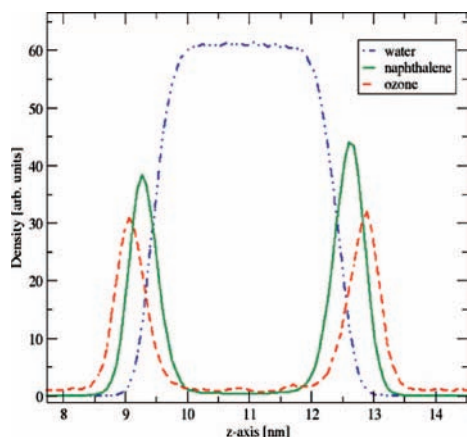
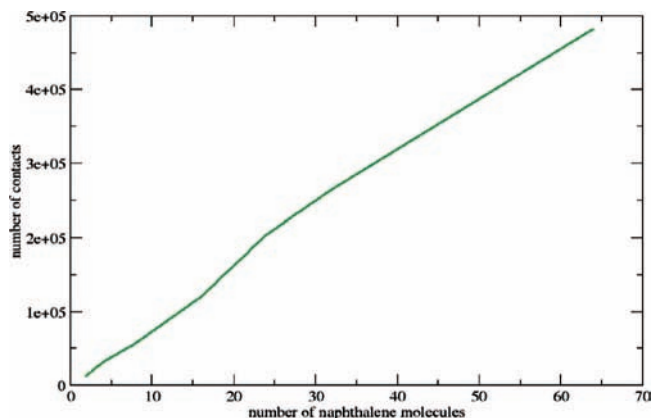
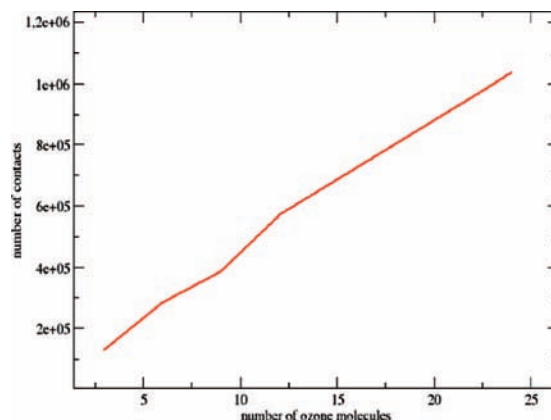
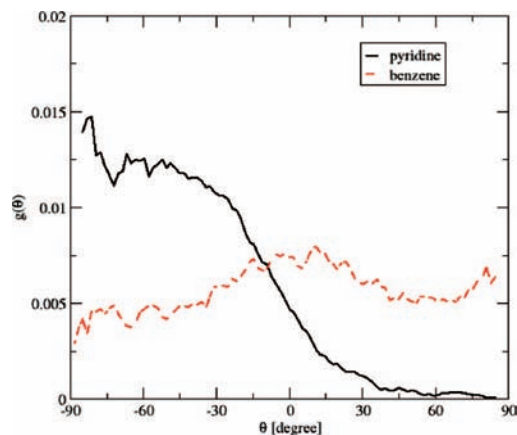
TABLE 3: Results of Quickstep Benchmarking against CCSD(T)/CBS for the Benzene–Water and Pyridine–Water Binary Complexes (Interaction Energies in kcal/mol)

complex	BLYP/DZVP	BLYP/DZVP+ Dispersion	CCSD(T)/CBS
benzene–water π -bonded	-1.87	-3.94	-3.28
pyridine–water π -bonded	-1.58	-3.69	-2.95
pyridine–water hydrogen-bonded	-6.97	-8.23	-7.24

calculation. Within the present implementation we used parameters derived recently for a similar setup (BLYP functional and 6-31G** basis set)³³ and did not employ periodic boundary conditions for the dispersion correction. This choice of parameters was verified by comparison of the performance of two basis sets for benzene–water and pyridine–water complexes. Interaction energies calculated using Quickstep at the BLYP/DZVP level with empirical dispersion were equally good, if not better than those from all-electron BLYP/6-31G** calculation when compared to benchmark data (CCSD(T)/CBS for benzene-water and pyridine-water clusters). The numerical results of this benchmarking, which shows a very satisfactory performance of the BLYP/DZVP method with empirical dispersion for the binary benzene-water and pyridine-water complexes, are presented in Table 3. In order to quantify the contribution of dispersion to studied interactions, we performed DFT-based symmetry adapted perturbation theory (SAPT) calculation at the PBE0AC/aug-cc-pVDZ level, which allowed us to decompose the total interaction energy to individual terms.

Ab initio MD simulations were performed using a unit cell of dimensions of $13.5 \times 15.6 \times 28.0$ Å, and we employed 2D slab periodic boundary conditions in x and y . For ab initio MD, where the computational bottleneck can be the number of plane waves (directly related to the size of the unit cell) this choice is more economic than the 3D boundary conditions employed for the classical MD. The unit cell consisted of 72 water molecules. A single aromatic molecule, either benzene or pyridine, was placed on one of the water/vapor interfaces of the slab. After initial equilibration of 1.5 ps, trajectories of 12 ps were collected within the NVT ensemble at 300 K.

For benzene we evaluated the distribution of angles θ between the aromatic plane and the water surface. This is equivalent to monitoring the angle between the normal to the aromatic ring

**Figure 2.** Density profiles of naphthalene, ozone, and water oxygen in a slab with unit cell containing 8 naphthalene, 6 ozone, and 809 water molecules.**Figure 3.** Number of contacts between naphthalene and ozone as a function of naphthalene concentration. The unit cell contained 6 ozone molecules.**Figure 4.** Number of contacts between naphthalene and ozone as a function of ozone concentration. The unit cell contained 32 naphthalene molecules, which roughly corresponds to monolayer coverage.**Figure 5.** Distribution of angles between the normal to the surface and the aromatic ring of benzene and pyridine obtained from classical molecular dynamics simulations. 0° corresponds to the aromatic ring lying flat on the surface, whereas $\pm 90^\circ$ means that the ring is perpendicular to the surface.

and the direction perpendicular to the water surface (i.e., the z -direction of the simulation box). This distribution was normalized using the $1/\sin(\theta)$ Jacobian factor. Technically, for pyridine, which has lower symmetry, we chose the C_1-N_4 vector to represent the aromatic ring, and monitored the angle between this vector and the z -axis. For the purpose of obtaining plots directly comparable to those for benzene, this angle was then shifted by 90° ; this angle is denoted by θ in the figures. Values

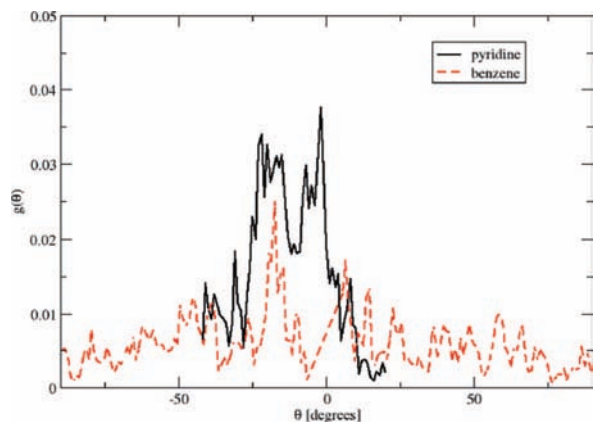


Figure 6. Distribution of angles between the normal to the surface and the aromatic ring of benzene and pyridine obtained from ab initio molecular dynamics simulations employing a DFT-D scheme.

were normalized using the $1/\sin(\theta-90^\circ)$ Jacobian factor. The use of normalization makes the analysis independent of the particular choice of aromatic molecule–water surface angle and, e.g., an isotropic orientational distribution of the aromatic molecule gives a constant distribution curve in our plots.

In order to investigate the importance of the dispersion correction for the benzene–water and pyridine–water interactions, we performed simulations both without and with this correction. In the former case, due to the lack of attractive dispersion interactions, the aromatic molecule underwent evaporation from water surface on the time scale of tens of femtoseconds, while in the latter case it correctly remained at the interface for the whole length of the simulation.

IV. Experimental Details

The UHV apparatus has been described in connection with our previous studies of the interaction of carboxylic acids with amorphous solid water (ASW).³⁴ Briefly, it includes facilities for valence-band electron-emission spectroscopy, metastable-impact electron spectroscopy (MIES), ultraviolet-photoelectron spectroscopy (UPS (HeI and II)), temperature-programmed desorption mass-spectroscopy (TPD), and reflection–absorption infrared spectroscopy (RAIRS). In this study we concentrate on RAIRS results. A few more detailed comments are added below concerning the application of RAIRS to the study of the molecular adsorption on films of solid water.

The ASW sample used as the substrate for the benzene or pyridine adsorption was prepared by deposition of water from the vapor phase on a polished polycrystalline silver disk held at 124 K. This disk is positioned in an exchangeable sample holder, which is mounted on an XYZ manipulator. The sample can be heated via a tungsten filament behind the silver disk or by electron bombardment. It can be cooled to 124 K by liquid-N₂ cooling facilities connected to the manipulator. The temperature was monitored with a tungsten–rhenium (26%–5%) thermocouple, clamped to the backside of the sample. Prior to the measurements, the Ag disk was sputtered with 2000 eV Ar⁺ ions at 500 K for periods of 30 min, followed by briefly annealing the sample to 750 K. The sample cleanliness was checked with Auger-electron spectroscopy after each cleaning cycle. Deuterated water (D₂O 99.8%) was used for the preparation of the ASW-films. All chemicals were purified by several freeze–pump–thaw cycles. The cleanliness of the employed liquids was checked by monitoring their mass spectra during adsorption measurements. The substrate was exposed to the vapor of the liquids by backfilling the chamber through different

leak valves, to prevent cross contamination in the gas line. All exposures are stated in Langmuir (L) ($1\text{ L} = 10^{-6}\text{ Torr s}$). The calibration of the L-scale in terms of the coverage of the surface by pyridine required auxiliary studies on the interaction of pyridine with Ag, described in detail in refs 35 and 36. The exposure-to-coverage relation is given in section V.

The grazing incidence reflection RAIRS setup contains a Bruker IFS 66v/S vacuum Fourier-transform infrared spectrometer, connected directly to the UHV chamber. The mid-IR beam, produced by a SiC-glowbar is focused by a KBr lens and enters the chamber through a differentially pumped KBr window. It is reflected under an angle of 83.5° to the Ag surface normal, and leaves the chamber through another KBr window. After passing a second KBr lens it is focused by a parabolic mirror onto a LN₂ cooled mercury cadmium telluride (MCT) detector, housed in a pumped stainless steel chamber. The region between 700 and 3500 cm^{-1} could be used for interpretation of the vibrational spectrum of the adsorbates. The spectra were recorded with a resolution of 4 cm^{-1} . 270 scans were added prior to the Fourier transformation and calculation of the absorbance as the negative logarithm of the ratio of a sample spectrum to a spectrum of the clean surface. Band intensities were evaluated from the peak heights (Figure 7) or peak areas (Figure 9) after the removal of the background under the peaks.

For RAIRS on benzene or pyridine layers, interacting with ASW deposited on silver we use the “buried metal-layer” approach.^{37,38} Thin films of benzene or pyridine (5 layers, thickness $<2\text{ nm}$, typically) are deposited on top of the highly reflecting polished silver substrate. It has been shown that the reflection and overall sensitivity of the experiment will be dominated by the optical properties of the metal substrate.^{37,38} On the other hand, the surface chemistry probed is that of the benzene (or pyridine)–ASW system. In addition, the metal surface selection rules still hold for these adsorption systems, allowing us to obtain information on the orientation of the aromatic molecules at the vacuum/water interface. More specifically, the RAIRS spectra provide information on the projection of the change in the net dipole moment of the molecule vibrating in given mode on the axis perpendicular to the metal surface, which correlates with the un-normalized orientation distributions (i.e., without the Jacobian factor being included) from the calculations.

V. Results

Computational. The surface segregation of benzene or small PAHs on water and ASW was already quantified in our previous work.^{15,35} Surface segregation of both naphthalene and ozone in the mixed system is best seen from density profiles of the individual species across the aqueous slab, averaged over the MD simulation, as depicted in Figure 2. Both naphthalene and ozone are surface active and almost do not penetrate into the aqueous bulk. Surface segregation of naphthalene, expressed either in terms of a surface density peak or free energy minimum, is stronger than that of ozone. At the same time, the latter species accumulates more on the vapor side of the interface than the former one. As a matter of fact, at higher naphthalene concentrations, when the surface is covered by the PAH, ozone molecules are exposed above the naphthalene layer almost without contact with water.

One of the purposes of the classical MD simulations of naphthalene and ozone on aqueous slabs was to investigate the contacts (possibly leading to ozonolysis reaction) between the two species. Numbers of these contacts, studied as a function of both naphthalene and ozone concentration are summarized

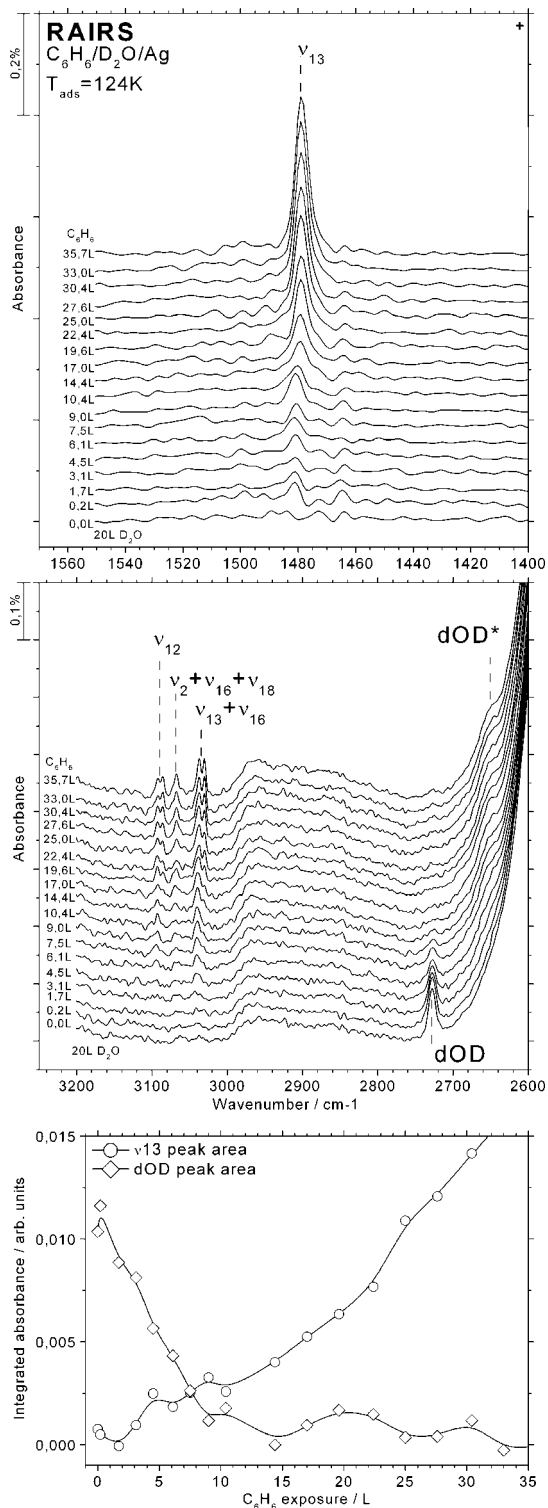


Figure 7. Top and middle panels: RAIRS spectra for D_2O films (5 ML) exposed to benzene at 124 K. Top: spectral region from 1400 to 1550 cm^{-1} ; Middle: spectral region from 2600 to 3250 cm^{-1} . Bottom panel: Activity of dOD of water and of ν_{13} of benzene.

in Figures 3 and 4. It can be seen from these figures that the dependence is roughly linear in both cases and we do not see saturation effects despite the broad concentration range for both ozone and naphthalene.

For reaction with incoming gaseous molecules the surface orientation of the aromatic molecule can be important. Figures 5 and 6 depict orientational distributions of a single benzene or pyridine molecule on a water slab obtained by classical and ab

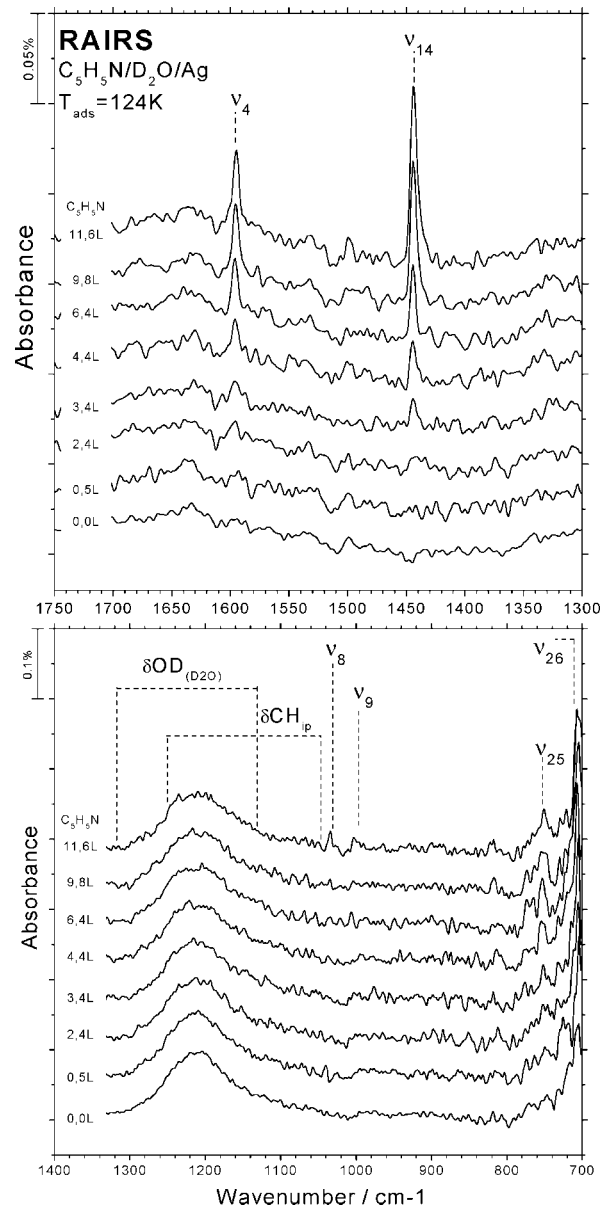


Figure 8. RAIRS spectra from the adsorption of pyridine on ASW at 124K (pyridine coverage up to about 1 ML).

initio MD. This is an important comparison which on the one hand checks the quality of the empirical force field while, on the other hand, establishes the necessary simulation time for reaching statistical convergence. Benzene weakly prefers to lie flat on the surface, however, all angles are populated. This indicates low barriers for rotational motions which can be overcome at 300 K, but probably not at 124 K. It can be expected that this leads to a more narrow orientational distribution for the case of benzene interacting with ASW (see below). The behavior of naphthalene is similar to that of benzene; here, the analysis of classical MD reveals a preferentially flat orientation with a significant angular flexibility. More precisely, naphthalene can almost freely rotate along a molecular axis passing through the two aromatic rings. However, rotation along an axis passing through the two carbon atoms shared by the two rings is much more hindered. Note that in our previous study, where we evaluated the potentials of mean force connected with moving these aromatic molecules across the air/water interface, preference for flat orientations was also observed, in particular for positions where the aromatic molecule

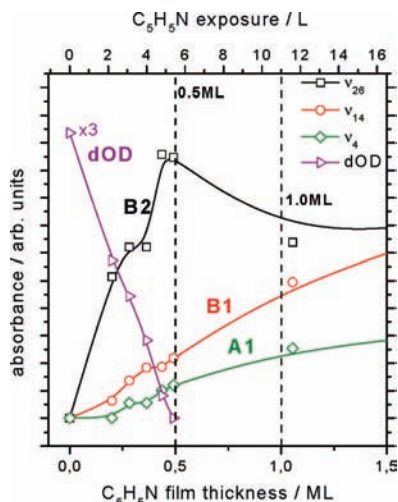


Figure 9. IR activity of the main pyridine modes, ν_4 , ν_{14} , and ν_{26} , versus the pyridine exposure on to ASW.

was lying right on the surface water layer.¹⁵ In contrast to benzene, pyridine is more oriented at the surface with the polar and strongly solvated nitrogen pointing into the aqueous phase and the aromatic ring being tilted with respect to the surface (Figures 5 and 6).

There is good agreement between results obtained for benzene from long classical MD simulations and shorter ab initio MD runs employing the newly developed DFT-D formalism. For pyridine, the agreement is reasonable with DFT-D predicting less tilted (more flat) ring geometries and a narrower distribution of angles than classical MD. The origin of this difference may be partly due to inaccuracies in the empirical force field but mainly due to limited sampling within the former calculations. Indeed, small angles were poorly sampled in the course of the necessarily short ab initio MD run.

The importance of inclusion of dispersion interactions into DFT is clearly illustrated by DFT-SAPT decomposition of interaction energy of three model clusters: π -bonded benzene–water and pyridine–water complexes, and the pyridine–water complex with a $N\cdots H$ hydrogen bond (see Table 4). In the case of π -bonded systems, dispersion is responsible for almost all of the interaction energy, and even in the hydrogen-bonded complex, it accounts for about 50% of it (Table 4). We conclude that for the studied systems dispersion can not be omitted from ab initio MD simulations. As a matter of fact, in a simulation without dispersion, benzene completely detaches and flies away from the water surface within a picosecond. DFT+D method fixes this problem without adding any appreciable computational expense on top of the DFT calculation.

Experimental. Interaction of Benzene with Silver and ASW Films on Silver. Table 5 relates the notation, used for the assignment of the detected benzene modes (i.e., Herzberg notation³⁹), to their symmetry. All infrared spectra of benzene shown in this article contain only bands of in-plane modes. Thus, these modes contribute to the IR absorption spectrum only if the molecular plane is tilted with respect to the surface. Note that for benzene, interacting with polycrystalline silver³⁵ (as with Cu(110)⁴⁰), any IR activity, from ν_{13} in particular, is clearly discernible only after the completion of the first layer. This is taken by us as an evidence that up to this stage the benzene ring plane is parallel to the silver substrate.⁴⁰

Figure 7 shows those parts of the RAIRS spectra for benzene on ASW (adapted from ref 30) that are most relevant for the following discussion. They are presented for exposures up to

36 L (corresponding to the completion of three adlayers). Note the water band dOD (2728 cm^{-1}), which originates from the OD stretch vibration of the dangling OD groups located at the ASW surface (middle panel). In addition, we detect IR absorption bands originating from internal vibrations in the benzene molecules (top and middle panel; see Table 4 for their assignment and characterization).

We observe a loss of intensity of dOD (2728 cm^{-1}) immediately after the start of the benzene exposure, while a broadband (around 2650 cm^{-1} , denoted as dOD*) emerges, being red-shifted by about 75 cm^{-1} relative to dOD. The dOD band disappears with the completion of the first adlayer while dOD* saturates. Thus, with the completion of the first adlayer all water dangling OD groups at the ASW surface are involved into bonds with benzene molecules.

Infrared absorption bands from the C–C and C–H stretch vibrations in the benzene molecule emerge around 3 L (corresponding to 0.3 ML benzene coverage). Above 5 L, additional activity from C–H stretch modes appears at 3068 and 3086 cm^{-1} (see Table 5). As all of these are in-plane modes, their activity must be attributed to benzene species that are tilted with respect to the water surface. Figure 7 (bottom panel) presents the intensity of dOD (water) and of ν_{13} (benzene) versus the benzene exposure. We interpret the absence of strong activity (below 3L) from in-plane modes, such as ν_{13} (1481 cm^{-1}), as indication that the species are oriented with their molecular plane preferentially parallel to the ASW surface, and that the orientation profile possesses a rather small width. The narrower distribution seen in the experiment compared to the calculations can be attributed to the significantly lower temperature at which the experiments were performed. Moreover, the standard normalization adapted for the simulation results (which might not fully reflect the experimental situation where different azimuthal angles contribute to the signal) leads to an optically broader distribution. Thus, the preference for parallel orientation of the benzene ring, seen in the experiment, is in agreement with simulation results.

Up to 3 L the number of dangling OD groups is reduced by 30% only, and the removal is not complete before 11 L. We explain the rise in the activity of in-plane modes observed between 6 and 11 L as follows: the integration of additional molecules into the first layer takes place, leading to the formation of a “compressed” monolayer. This requires a reorientation of the benzene molecules already present in order to accommodate more molecules. The molecules in the “compressed” first layer are then, on the average, oriented more upright which explains the increase of the intensity of ν_{13} for exposures higher than 6 L.

Interaction of Pyridine with Silver and ASW Films on Silver. Table 6 identifies and characterizes the pyridine-induced features seen between 700 and 1600 cm^{-1} . In the following the notation of ref 41 is used. Namely, modes of A1 and B1 symmetry are in-plane modes; thus, they are IR active only when the molecular plane is tilted with respect to the surface plane.

We have established earlier that pyridine stands upright when interacting with polycrystalline silver.³⁶ This was concluded from the fact that during the build-up of the first pyridine layer only the A1 modes of the skeletal (CC, CN) and the CH stretch vibrations, at 1592 and 3056 cm^{-1} , respectively, are seen. The B1 mode of the skeletal stretch vibration, at 1435 cm^{-1} , and the B2 mode of the CH out-of-plane bending vibration, at 752 cm^{-1} , are observed near the completion of the first and second layer, respectively. Should the pyridine molecular plane be parallel to the surface, only the B2 mode would be active.⁴⁰

TABLE 4: DFT-SAPT Decomposition of Benzene–Water and Pyridine–Water Interaction Energies (in kcal/mol)^a

complex	E_{Pol}^1	E_{I}^2	E_{D}^2	$\delta(\text{HF})$	ΔE	% of dispersion
benzene–water π -bonded	0.42	−0.57	−2.72	−0.34	−3.21	85
pyridine–water π -bonded	1.01	−0.55	−2.87	−0.33	−2.68	107
pyridine–water hydrogen-bonded	0.31	−2.19	−3.45	−1.52	−6.84	50

^a Notation of columns: polarization, E_{Pol}^1 ; induction (including exchange-induction), E_{I}^2 ; dispersion (including exchange-dispersion), E_{D}^2 ; higher order hartree-fock contributions, $\delta(\text{HF})$; total interaction energy, ΔE ; and percentual ratio of dispersion calculated as E_{D}^2 .

TABLE 5: Identification and Characterization of the Benzene Infrared Absorption Bands^a

ν_{p}	activity	$\text{C}_6\text{H}_6/\text{D}_2\text{O}$	
		chem.	phys.
2	R		
12	IR/R	3094	3092; 3086
13	IR/R	1481	1479
16	R		
18	R		
13 + 16		3040	3037; 3031
2 + 16 + 18		3068	3068

^a R, Raman active; IR, Infrared active; ν_{p} , mode notation according to ref 42; chem., band positions in chemisorbed layer; phys., band positions in physisorbed layers.

TABLE 6: Identification and Characterization of the Pyridine Infrared Absorption Bands^a

symmetry	ν_{p}	assignment ref 34	$\text{C}_5\text{H}_5\text{N}/\text{D}_2\text{O}$	
			chem.	phys.
A1	4	$\nu\text{CC}, \nu\text{CN}$	1595	1592; 1582
	6	δCH in plane		1219
	7	δCH in plane		1069
	8	ring breathing	1034	1034
	9	ring breathing	1002	994
B1	14	$\nu\text{CC}/ \nu\text{CN}$	1444	1442
	17	δCH in plane		1147
B2	25	δCH oop	751	753
	26	δCH in-phase oop	707	711

^a ν , stretching vibration; δ , bending vibration; ν_{p} , mode notation according to ref 35; oop, out of plane; chem., band positions in chemisorbed layer; phys., band positions in physisorbed layers.

According to the argumentation presented in refs 40 and 42, pyridine must be bound on silver via the N lone pair in the upright orientation.

The absorption band dOD (2728 cm^{-1}) from the OD stretch vibration, involving the dangling water OD groups (not reproduced here, but presented in ref 36) disappears at about 5 L (0.45 ML pyridine coverage), i.e., considerably earlier than for benzene interacting with ASW. This implies that already around 0.5 ML coverage all available dangling OD groups have become involved in pyridine–water hydrogen bonds.

Figure 8 presents the infrared absorption spectra of the pyridine/ASW system for pyridine exposures below 11 L, corresponding to the completion of the first pyridine adlayer (see top (bottom) panels for the A1 and B1 (B2) modes, respectively). IR absorption bands of pyridine can already be seen at rather low exposures studied (above 2 L, corresponding to 0.15 ML coverage). In contrast to pyridine on silver, the spectra in the submonolayer regime show considerable IR activity from the B2 out-of-plane mode at 751 cm^{-1} (as well as the B2 mode at 707 cm^{-1} which is, however, rather close to the detector cutoff), accompanied by a rather weak signal from the A1 mode at 1595 cm^{-1} (clearly seen above 4.4L). Comparatively strong emission is also seen from the B1 mode at 1444 cm^{-1} . The strong activity of B2 (as compared to A1)

modes in the initial stage of pyridine adsorption is an indication that the C_2 axis is not parallel to the surface normal (in contrast to silver), supporting the theoretical finding that both the nitrogen lone pair and also the formation of a π -hydrogen bond with water contribute to the pyridine–ASW bonding.

In the gas phase the intensity of the absorption bands ν_4 is larger than that of ν_{14} ,⁴³ whereas in the present case ν_4 is comparatively weak at low coverage. This fact, together with appreciable intensity of B2 modes, suggests pyridine orientations which peak at small tilt angles of the C_2 axis with respect to the surface plane with a relatively small width, in qualitative agreement with the MD calculations. Finally, the large activity of the B1 mode at 1444 cm^{-1} suggests a broad distribution of the pyridine molecular planes around the tilted C_2 axis.^{40,42}

Figure 9 displays the exposure dependence of the intensities of the most prominent bands (as derived from their peak areas). During the completion of the first layer, we observe a stagnation of the activity of the B2 mode while the IR activity of the in-plane modes further increases. This suggests that a coverage-driven reorientation of the pyridine molecules in the first layer takes place during its completion above 0.5 ML. Judging from the increase of the A1 activity, either the orientation profile of the pyridine molecules has become broader or all pyridine species stand now considerably more upright.

The relative intensity of the A1, B1, and B2 bands is governed by the orientation distribution of the molecule at the surface. As for benzene, it can be expected that the distribution narrows at the temperature of the experiment, peaking now at small angles. Thus, we have neglected the spread of the distribution during its following comparison with the relative RAIRS intensities. For the calculation of the relative mode intensities, we take furthermore into account that only these modes that possess a net dipole moment change with a component perpendicular to the surface are IR active; the required dynamical dipole moments can be found in ref 42. We find that the calculated intensities of the A1 to B2 modes are of the same order of magnitude. This is in satisfactory agreement with experiment, considering the facts that the B2 bands are located rather close to the cutoff of the IR detector, and that the width of the calculated orientation distributions was neglected.

VI. Discussion and Conclusions

Molecular dynamics simulations indicate that the primary tenet of the Langmuir–Hinshelwood kinetics mechanism, i.e., simultaneous adsorption of aromatic molecules and ozone holds at low and moderate concentrations, with the adsorption of the aromatic molecule being stronger and possibly inducing ozone adsorption in the vicinity. Surface coverage by PAHs, however, changes the effective structure of the surface and accessibility of water to the incoming ozone, which can affect the reactivity at the surface. This also implies that at higher surface coverages the Eley–Rideal picture of an incoming gas molecule reacting with an already adsorbed PAH may become applicable.

In particular at low coverages of aromatic molecules, it is also important to take into account the surface orientations of

these species as far as their reactivity is concerned. This is primarily due to the fact that aromatic molecules such as naphthalene may show different reactivity toward ozone, since ozonide formation is dependent on the detail of PAH-ozone interaction. Both simulations and experiments show that benzene prefers on average to lie flat on the surface, but it undergoes large scale angular motions and can even flip over (rotate). This rotation is more present at ambient temperatures (liquid simulations) than for the cryogenic ASW (experiments). Pyridine prefers orientations with nitrogen pointing into the aqueous phase and the aromatic ring tilted with respect to the aqueous surface. We stress that this direct comparison of experimental and theoretical information on the orientation profile of the water adsorbed molecules is rather unique. Within simulations, there is reasonable agreement between classical MD and ab initio MD with empirical dispersion. Dispersion interactions are important; without them aromatic molecules do not bind strong enough to water surface and, e.g., benzene desorbs fast. Analysis of classical MD simulations of naphthalene on water shows that it orients similarly to benzene. Namely, it prefers to lie flat on the surface, however, with a large angular flexibility, in particular along the axis passing through the two rings.

The simulations also showed that when the surface is covered by naphthalene, ozone adsorbs on top of it with almost no contact with water. In other words, the nonspecificity of the rates toward the nature of the surface can be explained as due to the relative positions of the adsorbate molecules. This affords an explanation for the weak dependence of the ozonolysis on the substrate. Simulations also show that there is sufficient degree of contacts between reactants, which can then lead to heterogeneous chemistry. However, within the present MD simulations the chemical reaction itself could not be directly simulated. It, therefore, remains to be investigated how the products can change the overall progress of the reaction.

Acknowledgment. Support from the Czech Ministry of Education (grant LC512) and from the US-NSF (Grant CHE 0431312) is gratefully acknowledged. R.V. thanks the Czech Science Foundation for support (Grant 203/05/H001). K.T.V. thanks the U. S. National Science Foundation for financial support (Grant No. ATM: 0355291). Part of the work in Prague was supported by Project Z40550506. PH acknowledges support via the Praemium Academie award.

References and Notes

- (1) Poschl, U.; Letzel, T.; Schauer, C.; Niessner, R. *J. Phys. Chem. A* **2001**, *105*, 4029.
- (2) Poschl, U. *J. Aerosol Medicine*. **2002**, *15*, 203.
- (3) Finlayson-Pitts, B. J.; Pitts, J. N. *Chemistry of the Upper and Lower Atmosphere*; Academic Press: New York, 2000.
- (4) ATSDR toxicological profile, parts 4 and 5; <http://www.atsdr.cdc.gov/toxprofiles/tp52.html>.
- (5) Eisele, F. L.; McDaniel, E. W. *J. Geophys. Res. [Atmos.]* **1986**, *91*, 5183.
- (6) Eisele, F. L. *J. Geophys. Res. [Atmos.]* **1988**, *93*, 716.
- (7) Eisele, F. L. *J. Geophys. Res. [Atmos.]* **1989**, *94*, 6309.
- (8) Tanner, D. J.; Eisele, F. L. *J. Geophys. Res. [Atmos.]* **1991**, *96*, 1023.
- (9) Zhao, Z.; Huskey, D. T.; Olsen, K. J.; Nicovich, J. M.; McKee, M. L.; Wine, P. H. *Phys. Chem. Chem. Phys.* **2007**, *9*, 4383.
- (10) Donaldson, D. J.; Mmerekki, B. T.; Chaudhuri, S. R.; Handley, S.; Oh, M. *Faraday Discuss.* **2005**, *130*, 227.
- (11) Mmerekki, B. T.; Donaldson, D. J.; Gilman, J. B.; Eliason, T. L.; Vaida, V. *Atmos. Environ.* **2004**, *38*, 6091.
- (12) Mmerekki, B. T.; Donaldson, D. J. *J. Phys. Chem. A* **2003**, *107*, 11038.
- (13) Vondracek, J.; Machala, M.; Minksova, K.; Blaha, L.; Murk, A. J.; Kozubik, A.; Hofmanova, J.; Hilscherova, K.; Ulrich, R.; Ciganek, M.; Neca, J.; Svrckova, D.; Holoubek, I. *Environ. Toxicol. Chem.* **2001**, *20*, 1499.
- (14) Raja, S.; Valsaraj, K. T. *Atmos. Res.* **2006**, *81*, 277.
- (15) Vacha, R.; Jungwirth, P.; Chen, J.; Valsaraj, K. T. *Phys. Chem. Chem. Phys.* **2006**, *8*, 4461.
- (16) Kahan, T. F.; Kwamena, N. O. A.; Donaldson, D. J. *J. Atmos. Environ. A* **2006**, *40*, 3448.
- (17) Partay, L.; Jedlovsky, P.; Hoang, P.; Picaud, S.; Mezei, M. *J. Phys. Chem. C* **2007**, *111*, 9407.
- (18) Kwamena, N.-O. A.; Staikova, M. G.; George, I. J.; Abbatt, J. P. D. *J. Phys. Chem. A* **2007**, *111*, 11050.
- (19) Perraudin, E. M.; Budzinski, H.; Villenave, E. *J. Atmos. Chem.* **2007**, *56*, 57.
- (20) McIntire, T. M.; Lea, A. S.; Gaspar, D. J.; Jaitly, N.; Dubowski, Y.; Li, Q. Q.; Finlayson-Pitts, B. J. *Phys. Chem. Chem. Phys.* **2005**, *7*, 3605.
- (21) Lindahl, E.; Hess, B.; van der Spoel, D. *J. Mol. Model.* **2001**, *7*, 306.
- (22) Vacha, R.; Slavicek, P.; Mucha, M.; Finlayson-Pitts, B. J.; Jungwirth, P. *J. Phys. Chem. A* **2004**, *108*, 11573.
- (23) Berendsen, H. J. C.; Grigera, J. R.; Straatsma, T. P. *J. Phys. Chem.* **1987**, *91*, 6269.
- (24) Jorgensen, W. L.; Maxwell, D. S.; Tirado-Rives, J. *J. Am. Chem. Soc.* **1996**, *118*, 11225.
- (25) Sander, R. Compilation of Henry's Law Constants for Inorganic and Organic Species of Potential Importance in Environmental Chemistry (Version 3), www.mpch-mainz.mpg.de/~sander/res/henry.html, 1999.
- (26) VandeVondele, J.; Krack, M.; Mohamed, F.; Parrinello, M.; Chassaing, T.; Hutter, J. *Comp. Phys. Comm.* **2005**, *167*, 103.
- (27) Goedecker, S.; Teter, M.; Hutter, J. *Phys. Rev. B* **1996**, *54*, 1703.
- (28) Kristyan, S.; Pulay, P. *Chem. Phys. Lett.* **1994**, *229*, 175.
- (29) Hobza, P.; Sponer, J.; Reschel, T. *J. Comput. Chem.* **1995**, *16*, 1315.
- (30) Zimmerli, U.; Parrinello, M.; Koumoutsakos, P. *J. Chem. Phys.* **2004**, *120*, 2693.
- (31) Grimme, S. *J. Comput. Chem.* **2004**, *25*, 1463.
- (32) Grimme, S. *J. Comput. Chem.* **2006**, *27*, 1787.
- (33) Jurecka, P.; Cerny, J.; Hobza, P.; Salahub, D. *J. Comput. Chem.* **2007**, *28*, 555.
- (34) Bahr, S.; Kempter, V. *J. Phys. Chem. C* **2007**, *111*, 11302.
- (35) Bahr, S.; Kempter, V. *J. Chem. Phys.* **2007**, *127*, 074707.
- (36) Bahr, S.; Kempter, V. *J. Chem. Phys.* **2007**, *127*, 174514.
- (37) Bermudez, V. M. *J. Vac. Sci. Technol. A* **1992**, *10*, 152.
- (38) Gardner, P.; LeVent, S.; Pilling, M. J. *Surf. Sci.* **2004**, *559*, 186.
- (39) Herzberg, G. *Infrared and Raman Spectra*; Van Nostrand: New York, 1956.
- (40) Haq, S.; King, D. A. *J. Phys. Chem.* **1996**, *100*, 16957.
- (41) Long, D. A.; Thomas, E. L. *Trans. Faraday Soc.* **1963**, *59*, 783.
- (42) Andersson, M. P.; Uvdal, P. *J. Phys. Chem. B* **2001**, *105*, 9458.
- (43) *NIST Chemistry WebBook, NIST Standard Reference Database Number 69*; Natl. Bur. Stand. Gaithersburg, MD, 2005; <http://webbook.nist.gov>.